Ultrafast Science
A SCIENCE PARTNER JOURNAL

RESEARCH ARTICLE

Broadband Diffractive Graphene Orbital Angular Momentum Metalens by Laser Nanoprinting

Guiyuan Cao[1,3], Han Lin[2,3*], and Baohua Jia[2,3*]

[1]Centre for Translational Atomaterials, School of Science, Swinburne University of Technology, John Street, Hawthorn, VIC 3122, Australia. [2]School of Science, RMIT University, 124 La Trobe Street, Melbourne, Victoria, 3000, Australia. [3]The Australian Research Council (ARC) Industrial Transformation Training Centre in Surface Engineering for Advanced Materials (SEAM), RMIT University, 124 La Trobe Street, Melbourne, Victoria, 3000, Australia.

*Address correspondence to: han.lin2@rmit.edu.au (H.L.); baohua.jia@rmit.edu.au (B.J.)

Citation: Cao G, Lin H, Jia B. Broadband Diffractive Graphene Orbital Angular Momentum Metalens by Laser Nanoprinting. *Ultrafast Sci.* 2023;3:Article 0018. https://doi.org/10.34133/ultrafastscience.0018

Submitted 12 December 2022
Accepted 18 January 2023
Published 15 March 2023

Optical beams carrying orbital angular momentum (OAM) play an important role in micro-/nanoparticle manipulation and information multiplexing in optical communications. Conventional OAM generation setups require bulky optical elements and are unsuitable for on-chip integration. OAM generators based on metasurfaces can achieve ultracompact designs. However, they generally have limited working bandwidth and require complex designs and multistep time-consuming fabrication processes. In comparison, graphene metalenses based on the diffraction principle have simple designs and can be fabricated by laser nanoprinting in a single step. Here, we demonstrate that a single ultrathin (200 nm) graphene OAM metalens can integrate OAM generation and high-resolution focusing functions in a broad bandwidth, covering the entire visible wavelength region. Broadband graphene OAM metalenses with flexibly controlled topological charges are analytically designed using the detour phase method considering the dispersionless feature of the graphene material and fabricated using ultrafast laser nanoprinting. The experimental results agree well with the theoretical predictions, which demonstrate the accuracy of the design method. The broadband graphene OAM metalenses can find broad applications in miniaturized and integrated photonic devices enabled by OAM beams.

Introduction

Optical vortex beams (OVBs) are optical light beams carrying orbital angular momentums (OAMs), which have been studied for decades since their discovery by Allen et al. [1] in 1992. An OVB has a helical wavefront with the phase expressed as $\exp(il\varphi)$, where φ is the azimuthal angle in the plane, and l is the topological charge. l can be any value between $-\infty$ and $+\infty$, the sign of which decides the handiness of the OAM. OAM beams carrying different integer topological charges are inherently orthogonal to each other, which enables a new degree of freedom for information encoding, data storage, and mode division multiplexing [2]. In addition, the helical wavefront results in a doughnut intensity profile of an OAM beam due to the destructive interference at the beam center, which provides a gradient force for trapping particles [3]. As a result, OAM beams have demonstrated broad applications, such as optical data storage [4], quantum information processing [5,6], optical communications [7], super-resolution imaging [8], and optical trapping [9] and manipulations [10,11]. Thus, developing simple and flexible methods and devices to generate optical OAM beams is highly desirable.

Various approaches and devices for OAM beam generation have been demonstrated, such as cylindrical lens mode converters [12,13], spatial light modulators [14], computer-generated holograms [15], and so on. These solutions have successfully generated different kinds of high-quality OAM beams and played a crucial role in both fundamental research and applications. However, the bulky volume and the cumbersome systems of these conventional OAM beam generators greatly limit their applications in integrated and miniaturized optical or photonic devices. Recently, new methods and devices based on periodically arranged 2-dimensional (2D) nanostructures, namely, metasurfaces [16–18], have been proved useful to achieve ultrathin and integratable OAM beam generators for high-quality OAM beams. However, they generally require complex and time-consuming iterative design methods to achieve accurate wavefront control [19,20], particularly in designing broadband metasurface lenses [21,22]. On the other hand, they also require multistep vacuum-based nanofabrication [23,24], including chemical vapor deposition, electron beam lithography, and pattern transfer processes [25,26], which are high-cost and time-consuming. Moreover, the metasurface structure designs have a relatively low tolerance for fabrication errors, especially for broadband designs.

In comparison, graphene metalenses with simple designs are based on the simultaneous phase and amplitude modulations enabled by a one-step laser nanoprinting [27–30]. They have demonstrated unique advantages of high-spatial-resolution focusing capability, ultrabroad working bandwidth, strong

mechanical strength, and resilience to harsh environment [31–33], which make them a promising candidate for diverse applications, including biomedical, integrated photonics, and optical communications [27,34–36]. Different from conventional materials, which can provide either amplitude or phase modulations, graphene materials can simultaneously manipulate the amplitude and phase of a light beam [31,37], allowing high flexibility and accuracy in the lens design to achieve desired focal intensity distributions. In our previous study, it has been demonstrated that graphene metalenses can be analytically designed using the Rayleigh–Sommerfeld and detour phase methods to achieve 3-dimensional (3D) light focusing without an iterative optimization process [33,38]. In addition, the designed graphene metalenses can be fabricated in a single step using a low-cost and scalable laser nanoprinting technique [39,40]. Therefore, graphene metalenses have attracted substantial research attention [41,42]. However, graphene metalenses with OAM beam generation and focusing functions using simultaneous phase and amplitude modulations have remained undeveloped.

This work proposes and demonstrates a new graphene metalens that can focus broadband OAM beams. The metalens is analytically designed using the detour phase technique, which combines a lens phase for focusing and a spiral phase for OAM generation. Therefore, the topological charge and the focal position of the generated OAM beam can be flexibly controlled. The designed metalenses are fabricated using ultrafast laser nanoprinting. The experimental focusing intensity distributions almost reproduce the theoretical predictions using the Rayleigh–Sommerfeld diffraction theory [38]. The demonstrated ultrathin graphene OAM metalenses provide a simple and cost-effective approach to achieve highly integrated and high-resolution OAM beam focusing. They will find broad applications in optical beam and particle manipulations, data storage, quantum information processing, and mode multiplexing communications in integrated photonic devices.

Materials and Methods

Spiral structures have been frequently employed as OAM generators [43]. However, these designs yield propagating OVBs instead of tightly focused OVBs that are essential for optical trapping and manipulation. Our graphene OAM metalens can tightly focus broadband optical plane waves into OVBs with a doughnut-shaped focal spot. The schematic of the broadband graphene OAM metalens design is shown in Fig. 1. The black spiral lines represent a reduced graphene oxide (rGO), and other parts represent a graphene oxide (GO) film [31]. The intensity and phase distributions in the focal region are shown in the insets. The graphene OAM metalens is designed using the detour phase technique to combine a lens phase for focusing and a spiral phase for OAM generation. Therefore, the focal positions and topological charges of tightly focused OVBs can be independently designed and flexibly controlled in a single-graphene OAM metalens.

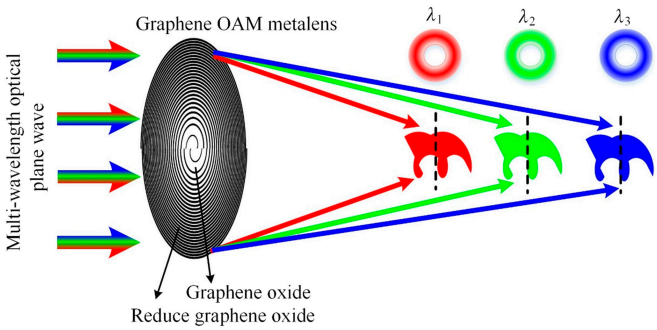

Fig. 1. Conceptual design of a broadband graphene OAM metalens that focuses different wavelengths at different positions with desired topological charges.

The detour phase technique is a method to modulate the wavefront by slightly changing the lateral locations of the apertures in the pupil plane [41,44], which has been widely used in holography [45], optical signal processing [46], and lens design [33]. The detailed design process is as follows. First, a graphene metalens with a focal length of f is targeted, consisting of concentric annular rGO rings, as shown in Fig. 2 (a2). To achieve constructive interference in the focal region, the radii of each ring can be expressed as $r_n = \sqrt{nf\lambda}$, where n is an integer and λ is the wavelength of the incident beam [38,47]. This design allows the metalens to work in a broad wavelength region. On the other hand, to generate an OAM with a topological charge l, the phase distribution of the spiral phase can be expressed by the following equation:

$$\phi(x,y) = l * \operatorname{atan}(y/x).$$

According to the detour phase technique, the lateral shift of the ring position can be defined as a function of the desired phase value:

$$\Delta d(x,y) = mod\left(\phi(x,y) + \Delta\varphi, 2\pi\right). * \frac{\lambda}{2\pi \sin\left(\operatorname{atan}\left(\sqrt{x^2+y^2}/f\right)\right)}, \quad (1)$$

where $\Delta\varphi$ is the phase modulation between GO and rGO zones, derived from the decrease in film thickness, and the refractive index increases when GO is reduced to rGO via the photoreduction process of the laser nanoprinting [27,29]. Because of the large refractive index difference between GO and rGO, only a very thin (200 nm) layer of GO is required to achieve the desired phase modulation after laser reduction, making the designed OAM metalens superior for various integrated photonic applications.

The graphene OAM metalens design process is shown in Fig. 2A, where the 3 insets (a1, a2, and a3) are under the same coordinate system. When adding a phase $\phi(x,y) + \Delta\varphi$ to the graphene metalens in a1 (the topological charge is 3), this phase $\phi(x,y) + \Delta\varphi$ at point (x, y) will lead to a location shift $\Delta d(x,y)$, which will result in the shift of point (x, y) in the graphene metalens plane to point (x', y') along the red dashed line. Therefore, a corresponding lateral shift $\Delta d(x,y)$ will be applied to the annular ring's radius $r_n(x,y)$ in the graphene metalens. Moreover, a new structure, namely, the graphene OAM metalens, can be obtained as shown in Fig. 2 (a3). The new radii become:

$$R_n(x',y') = r_n(x,y) + \Delta d(x,y). \quad (2)$$

Here, $R_n(x', y') = \sqrt{x'^2 + y'^2}$, $r_n(x, y) = \sqrt{x^2 + y^2}$.

Furthermore, considering the paraxial approximation of the lens design theory [48], $\sin\left(\operatorname{atan}\left(\sqrt{x^2+y^2}/f\right)\right)$ in Eq. 1 can

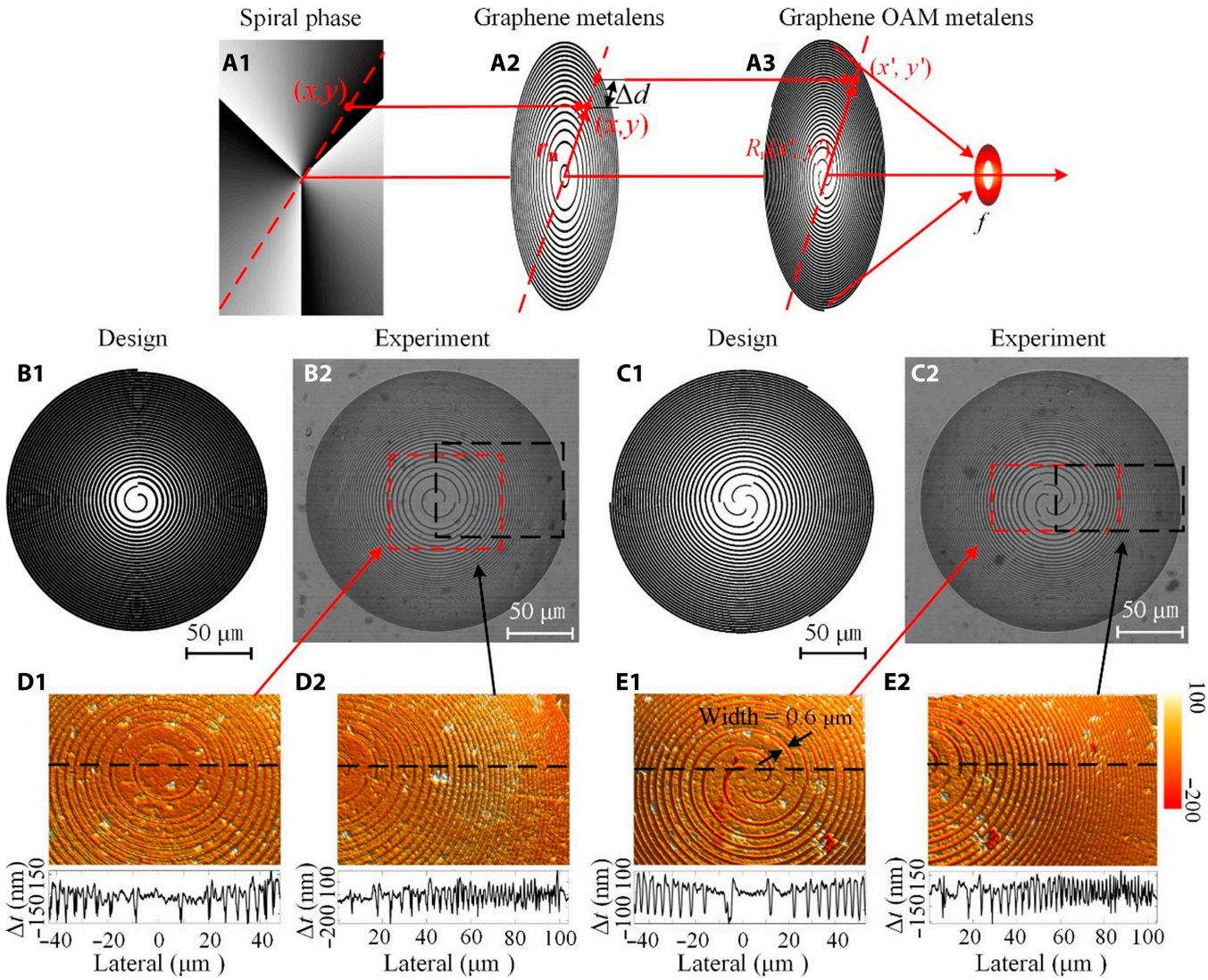

Fig. 2. Schematics of a graphene OAM metalens combining a graphene metalens with the spiral phase of a topological charge $l = 3$ based on the detour phase method. (a1) Spiral phase with $l = 3$. (a2) Schematic of a graphene metalens. (a3) Schematic of a graphene OAM metalens. Structure design (b1) and microscopic image (b2) of a fabricated graphene OAM metalens with a topological charge of 1. Structure design (c1) and microscopic image (c2) of a fabricated graphene OAM metalens with a topological charge of 3. (d1 and d2) Optical profiler images of the fabricated graphene OAM metalens in b2 in the red and black rectangles and cross-sectional plots marked by the black dashed lines. (e1 and e2) Optical profiler images of the graphene OAM metalens in c2 in the red and black rectangles and cross-sectional plots marked by the black dashed lines.

be approximated to $\sqrt{x^2+y^2}/f$, and the relationship between focal length f and wavelength λ for a graphene metalens can be expressed as $f = R/\lambda$, where R is a constant related to the radius of the graphene metalens [41,49]. Therefore, the equation of position shift $\Delta d(x, y)$ can be simplified as:

$$\Delta d(x,y) = mod\left(\phi(x,y) + \Delta\varphi, 2\pi\right). * \frac{R}{2\pi\sqrt{x^2+y^2}}. \quad (3)$$

From Eq. 3, it is easy to find out that the ring position shift is only related to the coordinate position and the radius of the graphene metalens. Therefore, the new radii $R_n(x', y')$ are not affected by wavelength, which grants graphene OAM metalens broadband working capability under the paraxial approximation. As shown in Fig. 2 (b1) and (c1), by using this approach, we designed 2 graphene OAM metalenses ($l = 1$ and $l = 3$) working at 633 nm. The focal length and the diameter of both metalenses are 200 μm.

Results

Laser nanoprinting [29,50] using a femtosecond laser (220-fs pulse width at 515 nm; NanoPrint3D, Innofocus Photonics Technology) was used to fabricate the 2 graphene OAM metalenses on a 200-nm-thick GO film, prepared by using the filtration method [51]. More importantly, femtosecond laser nanoprinting [52–54] can achieve higher resolution and well-controlled structures by the multiphoton effect with minimized heat generation, which makes it significantly different from laser processing with continuous wave, picosecond, or nanosecond lasers relying on heat generation. The microscopic images of the fabricated metalenses are shown in Fig. 2 (b2) and (c2). The structure morphologies of these 2 graphene OAM

metalenses were measured using an optical profiler. The images shown in Fig. 2 (d1), (d2), (e1), and (e2) are the structures in the areas marked by the red and black rectangles, respectively. In addition, the line graphs in these figures are the cross-sectional plots along the black dashed lines. The laser nanoprinting introduces a 100-nm decrease in the GO film thickness with a Gaussian profile, which facilitates the desired diffraction [31,38]. The width of the Gaussian-profiled rGO lines is ~0.6 μm as shown in Fig. 2 (e1). It is clearly seen from Fig. 2 that the fabricated structures almost reproduce the designs with well-defined concentric rings and high-resolution patterns enabled by the ultrafast nanoprinting process. These accurate fabrication outcomes are essential for the precise control of the wavefront.

A customized imaging system is used to measure the intensity distributions of these 2 graphene OAM metalenses, as shown in Fig. 3. A supercontinuum laser passes a 633-nm filter (with a bandwidth of 10 nm), and it is expanded to a beam diameter of ~5 mm as the incident beam. The diameter of the laser beam is much larger than the diameter (200 μm) of the graphene OAM metalenses as a uniform plane wave illumination. A 4*f* imaging system composed of a microscopic objective (numerical aperture (NA) = 0.8, 100×) and a tube lens (f = 200 mm) is used to image the focal intensity distributions of the metalenses using a charge-coupled device camera. The objective is mounted on a high-accuracy 1D piezo scanning stage (with an accuracy of 10 nm), which scans along the z axis. Therefore, the 3D focal intensity distributions of the graphene OAM metalenses can be captured and reconstructed by taking a series of images of the intensity distributions in the x–y planes along different z positions.

The measured focal intensity distributions at 633 nm are shown in Fig. 4 and compared with the theoretical results calculated using the Rayleigh–Sommerfeld diffraction theory [38]. The theoretical and experimental intensity distributions in the x–y plane of the graphene OAM metalenses with topological charges of 1 and 3 are shown in Fig. 4 (a1) and (a2), respectively, and the x–y planes are the focal planes corresponding to the white dashed lines in Fig. 4 (b1 and b2). The doughnut-shaped focal spots at the focal plane can be clearly identified in the figures. The intensity distributions (Fig. 4 (b1) and (b2)) in the x–z plane demonstrate that the accurate focal length (f = 200 μm) has been achieved.

From both sets of images, one can see that the experimental results agree very well with the theoretical designs, confirming the high accuracy of the design method, which can also be verified by the cross-sectional intensity plots in Fig. 4 (c1) and (c2). Compared to the theoretical results, the background of the experimental results is slightly higher due to the scattered laser light. In the case of the topological charge of l = 1, the diameters of the peak intensity on the doughnuts (marked by the black dashed lines in Fig. 4 (c1)) are 0.94 and 1.03 μm in theory and experiment, respectively. The deviation is only 8.7%. Meanwhile, in the case of l = 3, the diameters are 2.20 and 2.37 μm in theory and experiment, respectively. The deviation is 7.1%. As expected, the larger topological charge l is evidenced by the larger doughnut. These small differences between experiments and theory again manifest the design method's outstanding accuracy and the fabrication's high precision, which can lead to the desired high quality of the OAM beams.

To demonstrate the broadband working ability, we selected 7 filters at central wavelengths of 450, 500, 550, 600, 650, 700, and 750 nm. All the filters have a bandwidth of 50 nm. Therefore, the 7 filters cover the entire visible wavelength region. The graphene OAM metalens focuses the incident beams at different wavelengths to different axial positions. The position of the metalens is tuned to measure the focal intensity distributions. The resulting intensity distributions at different wavelengths in the focal planes are shown in Fig. 5. The top 2 rows are the focal intensity distributions and the cross-sectional plots of the graphene OAM metalens with a topological charge of l = 1. Meanwhile, the bottom 2 rows show the case of the graphene OAM metalens with a topological charge of l = 3. The well-defined doughnut-shaped focal spots from both metalenses can be clearly identified for all the wavelengths, demonstrating the effectiveness and accuracy of our design. The diameters (measurement error is ±0.07 μm) of these focal spots are listed in Table. As expected, the diameters of the OAM

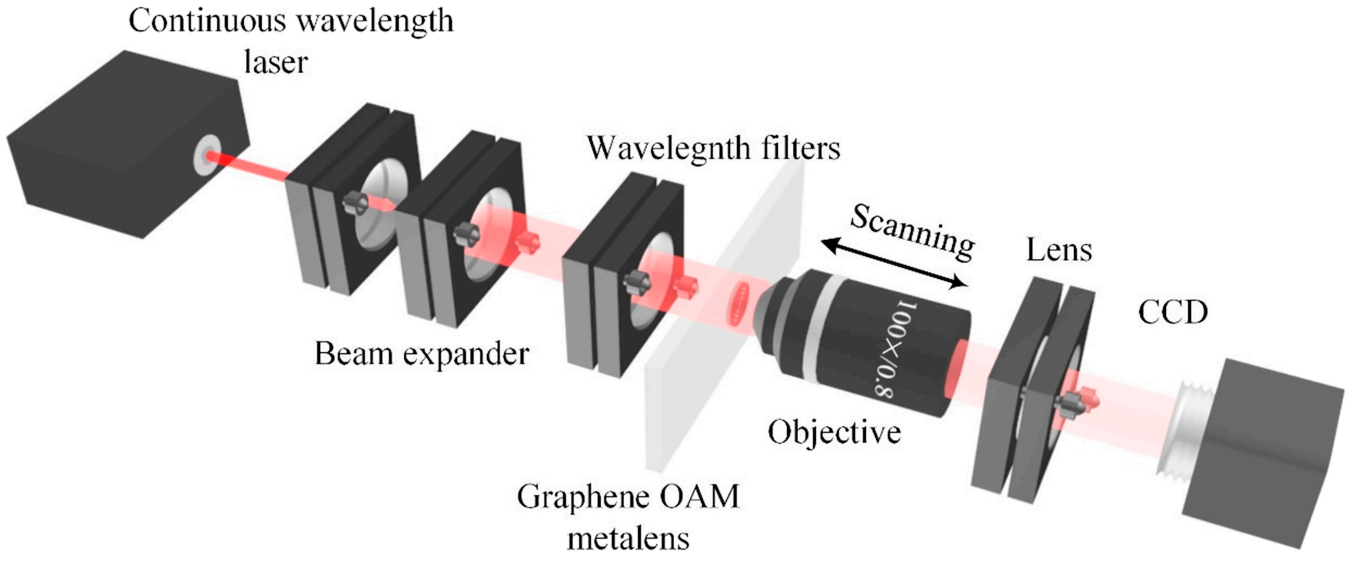

Fig. 3. 3D schematic of the imaging system for the characterization of the broadband graphene OAM metalenses. CCD, charge-coupled device.

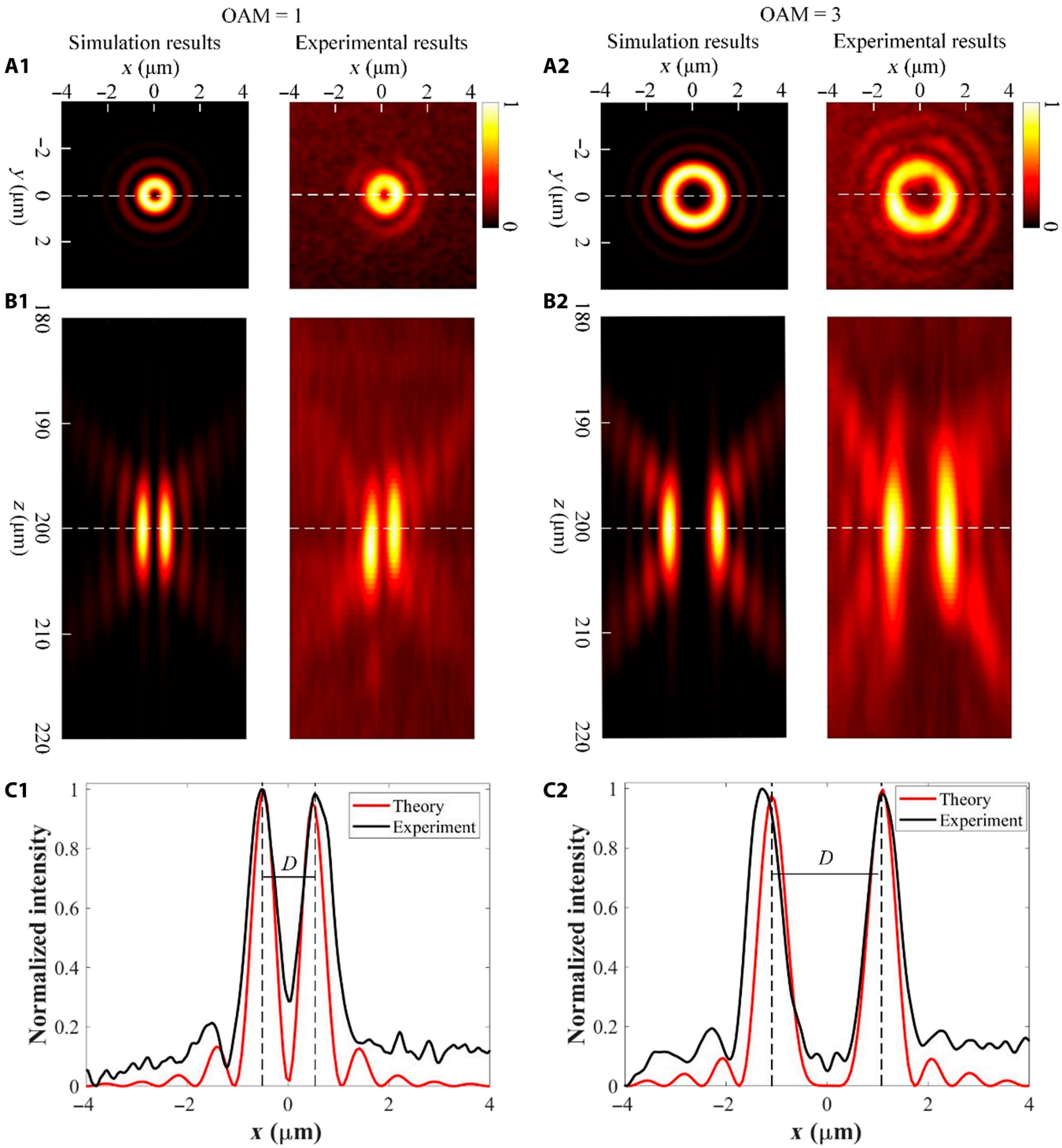

Fig. 4. Comparison between theoretical and experimental results of the 2 graphene OAM metalenses. The theoretical and experimental intensity distributions in the *x*–*y* plane of the graphene OAM metalenses with topological charges of $l = 1$ (a1) and $l = 3$ (a2). The theoretical and experimental intensity distributions in the *x*–*z* plane of the graphene OAM metalenses with topological charges of $l = 1$ (b1) and $l = 3$ (b2). (c1 and c2) The cross-sectional plots along the white dashed lines in (a1) and (a2), respectively.

beams with $l = 1$ are smaller than those with $l = 3$, which remain unchanged at different wavelengths, as shown in the bottom chart of Fig. 5. The diameter of the doughnut-shaped focal spot can be expressed as $d = \lambda/2\mathrm{NA}$, where $\mathrm{NA} = R_{max}/f$ is the numerical aperture of the metalens. Here, the R_{max} is the radius of the outmost ring of the metalens. Meanwhile, $f = R/\lambda$, as we discussed in the previous section, where R is a constant. Therefore, d is independent of the incident wavelength λ. As a result, broadband working ability in the whole visible band of our graphene OAM metalens has been demonstrated experimentally.

Conclusion

We have experimentally demonstrated broadband ultrathin graphene OAM metalenses with different topological charges

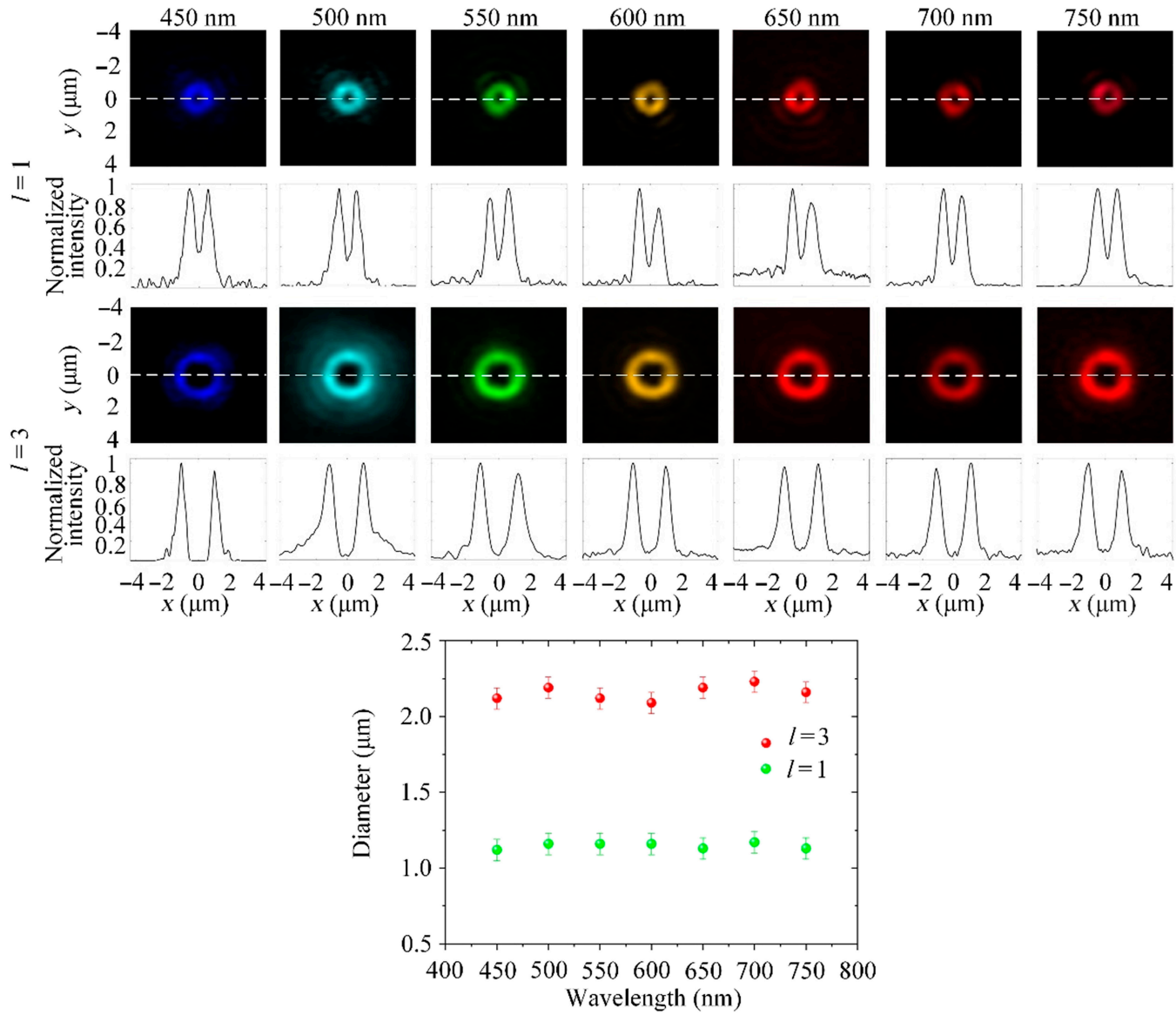

Fig. 5. The experimental measured focal intensity distributions of the 2 graphene OAM metalenses working at different wavelengths. The first row is the focal intensity distribution of the graphene OAM metalens with $l = 1$, and the second row is the cross-sectional plots along the white dashed lines in the first row. The third row is the focal intensity distribution of the graphene OAM metalens with $l = 3$, and the fourth row is the cross-sectional plots along the white dashed lines in the third row. The chart shows the unchanged diameter of the doughnut-shaped focal spots for both $l = 1$ and $l = 3$ with different incident wavelengths.

Table. The diameter (μm) of the doughnut-shaped focal spot.

	450 nm	500 nm	550 nm	600 nm	650 nm	700 nm	750 nm
$l = 1$	1.12	1.16	1.16	1.16	1.13	1.17	1.13
$l = 3$	2.12	2.19	2.12	2.09	2.19	2.23	2.16

and high-resolution focusing capability. A new method based on the detour phase technique and unique optical properties of GO has been developed to design the graphene OAM metalenses, which can independently control the focusing properties and the topological charge of the OAM at the same time. The accuracy of the design method is further confirmed by high-resolution 3D imaging of the graphene OAM metalenses fabricated by laser nanoprinting. Furthermore, the broadband ability of our graphene OAM metalens is demonstrated by focusing optical light beams at different wavelengths covering the entire visible range. Thus, the demonstrated method is versatile in designing different OAM metalenses. Moreover, the resulted dual-function graphene OAM metalenses are promising for broad applications in integrated optical and photonic devices using OAM beams. For these applications, such as optical trapping and manipulations, optical data storage, and quantum information processing, a smaller diameter of the doughnut-shaped spot is desired as it will be very useful to improve their performance. The design principle of graphene OAM metalens is based on the combination of graphene metalens and spiral phase loading. Therefore, the methods that

improve fabrication, increase the metalens size, or use other 2D materials with higher refractive index contrast are possible to reduce the doughnut-shaped spot size to a certain extent. However, the minimum diameter of the doughnut-shaped spot of graphene OAM metalens follows the diffraction limit, which means that there is a minimum size. To further reduce the spot size, the new design method should be proposed and implemented, maybe the combination of super oscillation metalens and spiral phase loading is one of the possible methods.

Acknowledgments

Funding: This work was supported by the Australia Research Council (grant no. DP220100603, FT210100806, and FT220100559), the Industrial Transformation Training Centres scheme (grant no. IC180100005), and Linkage Project scheme (LP210200345).
Competing interests: The authors declare that they have no competing interests.

Data Availability

The corresponding author can provide relevant data if the demand is reasonable.

References

1. Allen L, Beijersbergen MW, Spreeuw RJC, Woerdman JP. Orbital angular momentum of light and the transformation of Laguerre-Gaussian laser modes. *Phys Rev A*. 1992;45(11):8185.
2. Yan Y, Yue Y, Huang H, Ren Y, Ahmed N, Tur M, Dolinar S, Willner A. Multicasting in a spatial division multiplexing system based on optical orbital angular momentum. *Opt Lett*. 2013;38(19):3930–3933.
3. He H, Heckenberg N, Rubinsztein-Dunlop H. Optical particle trapping with higher-order doughnut beams produced using high efficiency computer generated holograms. *J Mod Opt*. 1995;42(1):217–223.
4. Voogd RJ, Singh M, Braat JJ. The use of orbital angular momentum of light beams for optical data storage. *Proc SPIE*. 2004;5380:387–392.
5. Vaziri A, Weihs G, Zeilinger A. Experimental two-photon, three-dimensional entanglement for quantum communication. *Phys Rev Lett*. 2002;89(24):Article 240401.
6. Zou X, Mathis W. Scheme for optical implementation of orbital angular momentum beam splitter of a light beam and its application in quantum information processing. *Phys Rev A*. 2005;71(4):Article 042324.
7. Bozinovic N, Yue Y, Ren Y, Tur M, Kristensen P, Huang H, Willner AE, Ramachandran S. Terabit-scale orbital angular momentum mode division multiplexing in fibers. *Science*. 2013;340(6140):1545–1548.
8. Tamburini F, Anzolin G, Umbriaco G, Bianchini A, Barbieri C. Overcoming the Rayleigh criterion limit with optical vortices. *Phys Rev Lett*. 2006;97(16):Article 163903.
9. MacDonald MP, Paterson L, Volke-Sepulveda K, Arlt J, Sibbett W, Dholakia K. Creation and manipulation of three-dimensional optically trapped structures. *Science*. 2002;296(5570):1101–1103.
10. Padgett M, Bowman R. Tweezers with a twist. *Nat Photonics*. 2011;5(6):343–348.
11. Molina-Terriza G, Torres JP, Torner L. Twisted photons. *Nat Phys*. 2007;3(5):305–310.
12. Beijersbergen MW, Allen L, van der Veen HELO, Woerdman JP. Astigmatic laser mode converters and transfer of orbital angular momentum. *Opt Commun*. 1993;96(1–3):123–132.
13. Padgett M, Allen L. Orbital angular momentum exchange in cylindrical-lens mode converters. *J Opt B Quantum Semiclassical Opt*. 2002;4(2):S17.
14. Gibson G, Courtial J, Padgett MJ, Vasnetsov M, Pas'ko V, Barnett SM, Franke-Arnold S. Free-space information transfer using light beams carrying orbital angular momentum. *Opt Express*. 2004;12(22):5448–5456.
15. Arlt J, Dholakia K, Allen L, Padgett MJ. The production of multiringed Laguerre–Gaussian modes by computer-generated holograms. *J Mod Opt*. 1998;45(6):1231–1237.
16. Karimi E, Schulz SA, de Leon I, Qassim H, Upham J, Boyd RW. Generating optical orbital angular momentum at visible wavelengths using a plasmonic metasurface. *Light Sci Appl*. 2014;3(5):e167.
17. Ren H, Briere G, Fang X, Ni P, Sawant R, Héron S, Chenot S, Vézian S, Damilano B, Brändli V, et al. Metasurface orbital angular momentum holography. *Nat Commun*. 2019;10(1):Article 2986.
18. Chung H, Kim D, Choi E, Lee J. E-band metasurface-based orbital angular momentum multiplexing and demultiplexing. *Laser Photonics Rev*. 2022;16(6):Article 2100456.
19. Yu N, Genevet P, Kats MA, Aieta F, Tetienne JP, Capasso F, Gaburro Z. Light propagation with phase discontinuities: Generalized laws of reflection and refraction. *Science*. 2011;334(6054):333–337.
20. Kildishev AV, Boltasseva A, Shalaev VM. Planar photonics with metasurfaces. *Science*. 2013;339(6125):Article 1232009.
21. Wang S, Wu PC, Su V-C, Lai Y-C, Hung Chu C, Chen J-W, Lu S-H, Chen J, Xu B, Kuan C-H, et al. Broadband achromatic optical metasurface devices. *Nat Commun*. 2017;8(1):Article 187.
22. Chen WT, Zhu AY, Sisler J, Huang YW, Yousef KMA, Lee E, Qiu CW, Capasso F. Broadband achromatic metasurface-refractive optics. *Nano Lett*. 2018;18(12):7801–7808.
23. Khorasaninejad M, Chen WT, Devlin RC, Oh J, Zhu AY, Capasso F. Metalenses at visible wavelengths: Diffraction-limited focusing and subwavelength resolution imaging. *Science*. 2016;352(6290):1190–1194.
24. Wang Y, Chen Q, Yang W, Ji Z, Jin L, Ma X, Song Q, Boltasseva A, Han J, Shalaev VM, et al. High-efficiency broadband achromatic metalens for near-IR biological imaging window. *Nat Commun*. 2021;12(1):Article 5560.
25. Hu D, Wang X, Feng S, Ye J, Sun W, Kan Q, Klar PJ, Zhang Y. Ultrathin terahertz planar elements. *Adv Opt Mater*. 2013;1(2):186–191.
26. Khorasaninejad M, Shi Z, Zhu AY, Chen WT, Sanjeev V, Zaidi A, Capasso F. Achromatic metalens over 60 nm bandwidth in the visible and metalens with reverse chromatic dispersion. *Nano Lett*. 2017;17(3):1819–1824.
27. Lin H, Zhang Z, Zhang H, Lin K-T, Wen X, Liang Y, Fu Y, Lau AKT, Ma T, Qiu C-W, et al. Engineering van der Waals materials for advanced metaphotonics. *Chem Rev*. 2022;122(19):15204–15355.
28. Lin H, Xu ZQ, Cao G, Zhang Y, Zhou J, Wang Z, Wan Z, Liu Z, Loh KP, Qiu C-W, et al. Diffraction-limited imaging with monolayer 2D material-based ultrathin flat lenses. *Light Sci Appl*. 2020;9(1):Article 137.
29. Lin H, Lin KT, Yang T, Jia B. Graphene multilayer photonic metamaterials: Fundamentals and applications. *Adv Mater Technol*. 2021;6(5):2000963.

30. Yang T, Lin H, Jia B. Ultrafast direct laser writing of 2D materials for multifunctional photonics devices. *Chin Opt Lett*. 2020;18(2):Article 023601.
31. Zheng X, Jia B, Lin H, Qiu L, Li D, Gu M. Highly efficient and ultra-broadband graphene oxide ultrathin lenses with three-dimensional subwavelength focusing. *Nat Commun*. 2015;6(1):Article 8433.
32. Cao G, Lin H, Fraser S, Zheng X, del Rosal B, Gan Z, Wei S, Gan X, Jia B. Resilient graphene ultrathin flat lens in aerospace, chemical, and biological harsh environments. *ACS Appl Mater Interfaces*. 2019;11(22):20298–20303.
33. Wei S, Cao G, Lin H, Mu H, Liu W, Yuan X, Somekh M, Jia B. High tolerance detour-phase graphene-oxide flat lens. *Photonics Res*. 2021;9(12):2454–2463.
34. Qu Y, Wu J, Zhang Y, Jia L, Liang Y, Jia B, Moss DJ. Analysis of four-wave mixing in silicon nitride waveguides integrated with 2D layered graphene oxide films. *J Lightwave Technol*. 2021;39(9):2902–2910.
35. Wu J, Jia L, Zhang Y, Qu Y, Jia B, Moss DJ. Graphene oxide for integrated photonics and flat optics. *Adv Mater*. 2021;33(3):2006415.
36. Wu J, Lin H, Moss DJ, Loh KP, Jia B. Graphene oxide for photonics, electronics and optoelectronics. *Nat Rev Chem*. 2023.
37. Li X, Ren H, Chen X, Liu J, Li Q, Li C, Xue G, Jia J, Cao L, Sahu A, et al. Athermally photoreduced graphene oxides for three-dimensional holographic images. *Nat Commun*. 2015;6(1):Article 6984.
38. Cao G, Gan X, Lin H, Jia B. An accurate design of graphene oxide ultrathin flat lens based on Rayleigh-Sommerfeld theory. *Opto-Electron Adv*. 2018;1(7):Article 180012.
39. Lin H, Sturmberg BCP, Lin KT, Yang Y, Zheng X, Chong TK, de Sterke CM, Jia B. A 90-nm-thick graphene metamaterial for strong and extremely broadband absorption of unpolarized light. *Nat Photonics*. 2019;13(4):270–276.
40. Lin K-T, Lin H, Yang T, Jia B. Structured graphene metamaterial selective absorbers for high efficiency and omnidirectional solar thermal energy conversion. *Nat Commun*. 2020;11(1):Article 1389.
41. Wei S, Cao G, Lin H, Yuan X, Somekh M, Jia B. A varifocal graphene metalens for broadband zoom imaging covering the entire visible region. *ACS Nano*. 2021;15(3):4769–4776.
42. Li X, Wei S, Cao G, Lin H, Zhao Y, Jia B. Graphene metalens for particle nanotracking. *Photon Res*. 2020;8(8):1316–1322.
43. Wang H, Liu L, Zhou C, Xu J, Zhang M, Teng S, Cai Y. Vortex beam generation with variable topological charge based on a spiral slit. *Nano*. 2019;8(2):317–324.
44. Brown BR, Lohmann AW. Complex spatial filtering with binary masks. *Appl Opt*. 1966;5(6):967–969.
45. Min C, Liu J, Lei T, Si G, Xie Z, Lin J, du L, Yuan X. Plasmonic nano-slits assisted polarization selective detour phase meta-hologram. *Laser Photonics Rev*. 2016;10(6):978–985.
46. Poon T-C. *Digital holography and three-dimensional display: Principles and applications*. Berlin/Heidelberg (Germany): Springer Science & Business Media; 2006.
47. Yu Y-H, Tian ZN, Jiang T, Niu LG, Gao BR. Fabrication of large-scale multilevel phase-type Fresnel zone plate arrays by femtosecond laser direct writing. *Opt Commun*. 2016;362:69–72.
48. Gu M. *Advanced optical imaging theory*. Berlin/Heidelberg (Germany): Springer Science & Business Media; 2000. vol. 75.
49. Wang Y, Yun W, Jacobsen C. Achromatic Fresnel optics for wideband extreme-ultraviolet and X-ray imaging. *Nature*. 2003;424(6944):50–53.
50. Lin H, Jia B, Gu M. Dynamic generation of Debye diffraction-limited multifocal arrays for direct laser printing nanofabrication. *Opt Lett*. 2011;36(3):406–408.
51. Jin Z, Cao G, Wang H, Lin H, Jia B, Qiu CW. Broadband angular momentum cascade via a multifocal graphene vortex generator. *Chin Opt Lett*. 2022;20(10):Article 103602.
52. Lin Z, Hong M. Femtosecond laser precision engineering: From micron, submicron, to nanoscale. *Ultrafast Sci*. 2021;2021:Article 9783514.
53. Zhang Y, Jiang Q, Long M, Han R, Cao K, Zhang S, Feng D, Jia T, Sun Z, Qiu J, et al. Femtosecond laser-induced periodic structures: Mechanisms, techniques, and applications. *Opto-Electron Sci*. 2022;1:Article 220005.
54. Lin Z, Ji L, Hong M. Approximately 30 nm nanogroove formation on single crystalline silicon surface under pulsed nanosecond laser irradiation. *Nano Lett*. 2022;22(17):7005–7010.